October 1980

Computed cross sections for electron transfer in $Ba^+ + Ba^+$ collisions

Stanley J. Sramek
University of Nebraska - Lincoln

J.H. Macek
University of Nebraska - Lincoln

Gordon A. Gallup
UNL, ggallup1@unl.edu

Sramek, Stanley J.; Macek, J.H.; and Gallup, Gordon A., "Computed cross sections for electron transfer in $Ba^+ + Ba^+$ collisions " (1980). *Gordon Gallup Publications*. 14.
https://digitalcommons.unl.edu/physicsgallup/14

PHYSICAL REVIEW A VOLUME 22, NUMBER 4 OCTOBER 1980

Computed cross sections for electron transfer in $Ba^+ + Ba^+$ collisions

Stanley J. Sramek and J. H. Macek
Department of Physics, University of Nebraska, Lincoln, Nebraska 68588

G. A. Gallup
Department of Chemistry, University of Nebraska, Lincoln, Nebraska 68588

(Received 15 November 1979)

Cross sections have been computed for the electron-transfer process $Ba^+ + Ba^+ \rightarrow Ba + Ba^{++}$, for collision energies ranging from 25 to 500 keV. The straight-line classical-trajectory method has been used, with basis functions obtained by the multiconfiguration valence-bond method. Several numerical procedures applicable to future treatments of similar large systems were developed. The maximum cross-section value is found to be around $27\pi a_0^2$ (2.4×10^{-15} cm^2), and occurs near collision energy 500 keV. The system's transient behavior has also been studied in detail during the collision, and it has been found that most electron-transfer events involve migration of the electron across internuclear distances considerably larger than the ionic diameter.

I. INTRODUCTION

A. Purpose of calculation

The heavy-ion heating approach to inertial confinement fusion[1] requires that intense ion beams be electromagnetically manipulated over significant times and distances. In particular, some HIF schemes envision ring storage of these beams for considerable time intervals prior to their delivery onto a fusion pellet. Charge-changing collisions occurring in the stored beam will cause ion loss from it, and will seriously limit its useful lifetime if the cross sections are too large.

Electron transfer is expected to be one of the most important charge-changing results of heavy-ion collisions at energies of hundreds of keV, the range relevant to the fusion program. Very little theoretical or experimental work has been done concerning electron-transfer collisions at these energies between ions carrying large numbers of electrons, although knowledge of the cross sections is essential to the further development of the HIF concept.

We have therefore computed cross sections for the electron-transfer process $Ba^+ + Ba^+ \rightarrow Ba + Ba^{++}$, for collision energies ranging from 25 to 500 keV. Our purpose was to obtain reliable cross sections based on accepted state-of-the-art *ab initio* theory, and to gain a qualitative understanding of the physical processes occurring during the collisions. We chose the $Ba^+ + Ba^+$ system because each ion has an unpaired loosely-bound outer electron; we expect that these electrons will participate in charge-changing events so readily that this system should represent very nearly a worst possible case for applicability to the fusion program.

B. Basic formalism

We have treated the $Ba^+ + Ba^+$ collision using the straight-line classical-trajectory method.[2] As basis states, we used molecular eigenstates obtained by the multiconfiguration valence-bond (MCVB) method.[3,4] To the best of our knowledge, our calculation is the first treatment, at this level of sophistication, of collisional electron transfer between such heavy ions.

The first step in our treatment, then, is to obtain a set of energies and eigenfunctions for the molecular system Ba_2^{++}, as functions of the distance between the two Ba nuclei. That is, we must obtain approximate solutions to the eigenvalue problem

$$\hat{H}(R)\psi_\mu(R) = E_\mu(R)\psi_\mu(R) , \tag{1}$$

where R is the internuclear separation, and the Hamiltonian $\hat{H}(R)$ includes the electron kinetic energies and all electron-electron, electron-nucleus, and nucleus-nucleus Coulomb interactions. (Throughout this paper we use notations of the forms $\hat{O}$, O, O_{nm}, respectively, for operators, matrices representing operators, and individual matrix elements of operators.) Relativistic effects are not included. All electron coordinates are treated quantum mechanically, but the nuclear coordinates are treated as fixed parameters of $\hat{H}(R)$. In solving Eq. (1), we use a space-fixed coordinate system with origin at the center of mass of the two nuclei. We compute solutions assuming that the two nuclei are located on this system's z axis. For homonuclear problems the two nuclei are thus located at positions $z = \pm\frac{1}{2}R$. The internuclear separation is written as a scalar R rather than as a vector $\vec{R}$ in Eq. (1)

because of this assumed restriction on the nuclear positions. The Hamiltonian $\hat{H}(R)$ and the wave functions $\psi_\mu(R)$, of course, also depend on all of the electron cordinates, but our notation suppresses this dependence. The subscript μ represents all symmetry indices and principle quantum numbers necessary to characterize the eigenfunction $\psi_\mu(R)$.

The functions $\psi_\mu(R)$ are then used as basis functions in solving the time-dependent Schrödinger equation

$$\hat{H}(\vec{R})\,\Psi(\vec{R},t)=i\frac{\partial}{\partial t}\Psi(\vec{R},t)\,. \tag{2}$$

The equation is written in atomic units, which are used throughout this paper unless otherwise specified. The internuclear separation is now a time-dependent vector,

$$\vec{R}=\vec{b}+\vec{v}t\,,$$

where $\vec{v}$ is the relative velocity of the two nuclei and $\vec{b}$ is a vector perpendicular to $\vec{v}$ whose magnitude b is called the *impact parameter*. We use the previously defined space-fixed coordinate system, with origin at the center of mass of the two nuclei. The vectors $\vec{v}$ and $\vec{b}$ are chosen to point in the $+z$ and $-x$ directions, respectively. The Hamiltonian $\hat{H}(\vec{R})$ is now time dependent, because the electron-nucleus and nucleus-nucleus Coulomb interactions depend on $\vec{R}$.

The wavefunction is written as an expansion,

$$\Psi(\vec{R},t)=\sum_\mu c_\mu(t)\,\Phi_\mu(\vec{R},t)\,, \tag{3}$$

where the $c_\mu(t)$ are unknown coefficients. The basis functions $\Phi_\mu(\vec{R},t)$ are obtained from the molecular eigenfunctions $\psi_\mu(R)$ by a simple time-dependent rotation and by multiplication by a translation factor,

$$\Phi_\mu(\vec{R},t)=\exp[-i\alpha_\mu(t)]\,\tau(\vec{R},t)\times\{\exp[-i\theta(t)\,\hat{J}_y]\,\psi_\mu(R)\}\,, \tag{4}$$

where $\hat{J}_y$ is the y component of the total electronic orbital angular momentum, and $\theta(t)$ is the angle between the z axis and the internuclear axis $\vec{R}$. The function $\exp(-i\theta\hat{J}_y)\,\psi_\mu$, produced by a simple rotation operation, is, of course, an eigenfunction of a molecule whose internuclear axis lies at an angle θ with respect to the z axis, rather than along the z axis. This use of rotating basis functions incorporates into our calculation the rotation of the internuclear axis through π radians during the collision.[5] We refer to $\psi_\mu(R)$ and $\Phi_\mu(\vec{R},t)$ as *nonrotated* and *rotated* functions, respectively, although the transformation of Eq. (4) involves more than just a rotation. The translation factor $\tau(\vec{R},t)$ assures that, in the $t\rightarrow\pm\infty$ limits, the uniform motion through space of the electronic cloud around each nucleus is properly represented by the wavefunction.[6] Our notation suppresses the dependence of $\tau(\vec{R},t)$ and $\Phi_\mu(\vec{R},t)$ on the electron coordinates. The phases $\alpha_\mu(t)$ are chosen for convenience:

$$\alpha_\mu(t)=\int_0^t E_\mu(R')\,dt'\,,$$

where

$$R'=|\vec{R}'|=|\vec{v}t'+\vec{b}|\,.$$

By substituting the expansion (3) into Eq. (2), and projecting onto $\langle\Phi_\mu|$, the usual dynamical equations for the unknown coefficients are obtained:

$$i\frac{dc_\mu}{dt}=\sum_\nu M_{\mu\nu}(\vec{R},t)\,c_\nu(t)\,, \tag{5}$$

where

$$M_{\mu\nu}(\vec{R},t)=\left\langle\Phi_\mu(\vec{R},t)\left|\left(\hat{H}(\vec{R})-i\frac{\partial}{\partial t}\right)\right|\Phi_\nu(\vec{R},t)\right\rangle\,. \tag{6}$$

The cross section for collisional transition from the system's initial eigenstate to molecular eigenstate μ is then, in units of πa_0^2,

$$\sigma_\mu(v)=2\int_0^\infty b\,P_\mu(v,b)\,db\,,$$

$$P_\mu(v,b)=\lim_{t\rightarrow+\infty}|c_\mu(t)|^2\,.$$

Throughout this paper our notation for transition probabilities and cross sections includes no subscript designating the initial state, because the system's ground state is always taken as the intitial state. The subscript μ always designates the final state.

This short review of the straight-line classical-trajectory method shows that our calculation divides naturally into three major computational steps. First, the molecular eigenstates and energies $\psi_\mu(R)$, $E_\mu(R)$ must be obtained by computing solutions to Eq. (1) as functions of R, using some appropriate method from molecular quantum mechanics. Second, these eigenstates and energies must be used to compute and tabulate numerical values for the functions $M_{\mu\nu}(\vec{R},t)$ [Eq. (6)]. Third, the set of coupled differential equations (5) must be repeatedly integrated numerically, using the tabulated $M_{\mu\nu}(\vec{R},t)$ as coupling-matrix elements, to obtain the transition probabilities $P_\mu(v,b)$ as functions of the relative nuclear speed and the impact parameter. Each of these three steps is described in greater detail in Secs. II, III, and IV. Within each section the theory, numerical methods, and results of one step are described in separate subsections.

Our use of the straight-line classical-trajectory description of the nuclear motion is easily justified. For example, at a collision energy of 200 keV the deBroglie wavelength associated with the nuclear motion of two Ba^+ ions is only $0.00015a_0$, so that the wave packet for the nuclear motion can be regarded as sharply localized and following a classical trajectory. The angular deflection of this classical motion due to the overall Coulomb repulsion between the ions only 0.000 07 radians for an impact parameter of $2a_0$, so that a straight-line trajectory is an excellent approximation.

There are two advantages gained by using molecular eigenstates rather than atomic eigenstates in this problem. First, the use of molecular eigenstates allows us to gain greater understanding of the physical processes occurring during the collision that lead to electron-transfer transitions. Second, the use of molecular eigenstates generally reduces the size of the set of coupled differential equations (5), because the expansion (3) need only include a few of the lowest-lying eigenstates.

II. MOLECULAR EIGENSTATES

A. Theory

To obtain the molecular eigenstates and energies $\psi_\mu(R)$, $E_\mu(R)$, we have used a specialized form of the MCVB procedure, which we call the *interpolated Hamiltonian* multiconfiguration valence-bond (IHMCVB) method. This method consists of five steps.

First, a set of one-electron basis functions $\{u_i(\vec{r},R)\}$ is chosen; $\vec{r}$ is the position of one electron. These functions, called *atomic orbitals* (AO's) are atom centered and, as R varies, move rigidly with one nucleus or the other without distortion.

Second, a set of multielectron basis functions $\{\phi_n(R)\}$ is constructed from the AO's. These functions, called *tableau symmetry functions* (TSF's) are constructed so that each has a definite exchange symmetry, spin multiplicity, and spatial symmetry.[3] Molecular eigenstates of a definite symmetry are obtained by using only those TSF's of that same symmetry.

Third, for each desired symmetry, the TSF's are used to compute a Hamiltonian matrix $H(R)$ and an overlap matrix $S(R)$:

$$H_{nm}(R)=\langle\phi_n(R)|\hat{H}(R)|\phi_m(R)\rangle\ ,$$
$$S_{nm}(R)=\langle\phi_n(R)|\phi_m(R)\rangle\ .$$

The overlap matrix is not diagonal because the AO's (and therefore the TSF's) are not orthogonal. Because a large number of two-electron integrals must be computed and manipulated, the numerical computation of $H(R)$ and $S(R)$ for a system as large as Ba_2^{++} consumes a large amount of computer time. Therefore, $H(R)$ and $S(R)$ are computed for a fairly small set of R values, called the *coarse grid*.

Fourth, a suitable interpolation scheme is devised, so that the $H(R)$ and $S(R)$ values computed on the coarse grid can be used to estimate $H(R)$ and $S(R)$ values accurately for intermediate R values. As explained below in Sec. III C, the piecewise analytic functions used in this interpolation must have continuous first *and second* derivatives across the boundaries defined by the coarse grid.

Fifth, the interpolated $H(R)$ and $S(R)$ matrices are used to solve the matrix eigenvalue problem

$$H(R)\,a_\mu(R)=E_\mu(R)\,S(R)\,a_\mu(R)\ . \qquad (7)$$

Solutions are computed for many more R values than are included in the coarse grid; this larger set of R values is called the *fine grid*. $a_\mu(R)$ is a column matrix whose elements, denoted $a_{n\mu}(R)$, define the molecular eigenstate

$$\psi_\mu(R)=\sum_n a_{n\mu}(R)\,\phi_n(R)\ . \qquad (8)$$

For our treatment of the Ba_2^{++} system, we chose a set of AO's consisting of 70 Gaussian-type orbitals (GTO's), 35 centered at each nucleus. Each GTO consists of a linear combination of the form

$$u_i(\vec{r},R)=N\sum_k b_{ki}\,g_i(\alpha_{ki},\vec{r},R)\ ,$$

where N is a normalizing factor and g_i is a Gaussian-lobe function[7] centered at one nucleus or the other. At each nuclear center, we used a (7s, 6p, 2d) set of AO's. Our values for α_{ki} and b_{ki} are listed in Table I.

We constructed TSF's for the Ba_2^{++} system according to the usual MCVB procedure.[3] The AO's $\{u_i\}$ were first transformed to a new set $\{w_i\}$. At each nuclear center, the $\{w_i\}$ were divided into a (5s, 4p, 2d) subset called *core orbitals*, and a (2s, 2p) subset called *valence orbitals*. The core orbitals were obtained as linear combinations of the $\{u_i\}$ using the Roothaan SCF procedure.[8] The valence orbitals were obtained by selecting the most spatially diffuse (2s, 2p) subset of $\{u_i\}$ and orthogonalizing it to the core orbitals, as prescribed by the MCVB procedure.

The procedure used in constructing the TSF's from the $\{w_i\}$ has been adequately described elsewhere.[3] Briefly, each TSF is a linear combination of products of Slater determinants formed from selected subsets of $\{w_i\}$. The manner of selecting orbitals and forming the linear combinations assures that each TSF has the desired molecular symmetry, that the core orbitals are always

TABLE I. The scaling factors α_{ki} and coefficients b_{ki} used in constructing each AO $u_i(\vec{r}, R)$. For each AO symmetry, the α values are listed in the first row of numbers and the b values are listed in the second row.

AO Symmetry	Scaling factors α Coefficients b		
1s	2273.6181	404.7034	
	0.4301	0.6789	
2s	144.9256	36.7570	
	0.1048	1.0260	
3s	90.9366	7.9295	
	−0.1530	1.0514	
4s	10.5220	1.7455	
	−0.3046	1.1469	
5s	1.0588	0.2735	
	−0.5117	1.3075	
6s	0.0221		
	1.0000		
7s	0.0084		
	1.0000		
2p	506.3780	90.1351	
	0.4301	0.6789	
3p	52.6800	13.3610	
	−0.1828	1.0365	
4p	26.6866	2.3270	
	−0.1530	1.0514	
5p	1.6841	0.2794	
	−0.3046	1.1469	
6p	0.2018		
	1.0000		
7p	0.0521		
	1.0000		
3d	148.0645	26.3554	12.0152
	0.4301	0.6789	1.4143
4d	3.0474		
	1.0000		

fully occupied, and that each TSF is either a *charge-equal* function or an *electron-transfer* function. Each Slater determinant in a charge-equal TSF is formed with equal numbers of electrons occupying orbitals centered at each nucleus. Each determinant in an electron-transfer TSF is formed with unequal numbers of electrons occupying orbitals centered at each nucleus.

For the Ba_2^{++} system, we constructed 26 TSF's of symmetry $^1\Sigma_g^+$ and 20 of symmetry $^3\Sigma_u^+$. These symmetries are the only ones that permit both Ba^+ ions to be in their ground states as $R \to \infty$. If the colliding ions are assumed to be in their ground states initially, and if the collisional couplings $M_{\mu\nu}(\vec{R}, t)$ are weak between states of unlike symmetry, then only these two symmetries must be included in the collision dynamics computations.

The matrices $H(R)$ and $S(R)$ were computed on the coarse grid using the method and programs of Gallup,[4] which are designed specifically for use with nonorthogonal TSF's. The choice of coarse grid R values, the interpolation method used to estimate $H(R)$ and $S(R)$ values on the fine grid, and the choice of fine grid R values are discussed in Sec. II B.

The use of interpolated $H(R)$ and $S(R)$ matrices is an important numerical technique applicable to future treatments of molecular systems similar in size to Ba_2^{++}. Some previous workers[9] have also used interpolated Hamiltonians in molecular calculations. The use of interpolated matrices is desirable for the following reason. Rapid variation of the molecular eigenstates with R, especially near avoided curve crossings, requires that eigenstates be obtained on a dense grid of R values. But the computation of exact values for $H(R)$ and $S(R)$ on such a dense grid is prohibitively expensive for so large a molecule; it is necessary to obtain approximate values. Because $H(R)$ and $S(R)$ vary fairly slowly and smoothly with R, it is convenient to obtain these approximate values by interpolating exact values computed on a coarse grid.

B. Numerical methods

The R values included in the coarse grid were (in atomic units) 3.0, 3.5, 4.0, 4.5, 5.0, 6.0, 7.0, 8.0, 9.0, 10.0, 11.0, 11.5, 12.0, 13.0, 14.0, 15.0, 16.0, 17.0, 18.0, 20.0, 22.0, 33.166248, and 50.0. Values smaller than 3.0 could not be treated because of numerical difficulties: For smaller distances the overlap between the most diffuse valence AO's of like symmetry type but centered on opposite nuclei became sufficiently close to unity that the $H(R)$ matrix became nearly singular. The matrix eigenvalue equation (7) then could not be solved accurately.

The matrices were interpolated using the following scheme. For $R < 22.0$, each matrix element was represented on each coarse grid interval by a fifth-order polynomial. Each polynomial matched the computed matrix-element values at the interval's endpoints, and also matched *preassigned* values of the element's first and second derivatives. These derivative values were assigned, after considerable numerical experimentation, by a simple procedure that assured a very smooth nonoscillatory fit to the computed points. For $R > 22.0$, several interpolation methods were used, because different groups of $H(R)$ and $S(R)$ matrix elements behave in radically different ways in the large-R limit. The nonconstant $S(R)$ elements approach their limiting values so rapidly that, for any element, the values on the three outermost coarse grid points are very nearly equal. We found through numerical experimentation that any attempt to interpolate these elements with continuous second derivatives resulted in unacceptable oscillatory behavior. Therefore, we interpolated these elements with linear polynomials on interval $[33.166248, 50.0]$ and with fourth-order polynomials on $[22.0, 33.166248]$. Use of this scheme assured continuity of the first derivatives and freedom from oscillations. The $H(R)$ elements were divided into two classes. The first class consisted of all elements in which either both TSF's involved were charge-equal functions, or both were electron-transfer functions. The second class consisted of all elements in which one TSF was a charge-equal function and one was an electron-transfer function. Because matrix elements of the first class, in the large-R limit, approach their limiting values as inverse powers of R, these elements were interpolated using polynomials in R^{-1}. Because elements of the second class approach their limiting values extremely rapidly, they were interpolated using the method used for $S(R)$.

We computed solutions to the matrix eigenvalue problem (7) on fine grids consisting of 119 points on the interval $[5.0, 50.0]$ for the ${}^1\Sigma_g^+$ symmetry and 173 points on the interval $[3.0, 50.0]$ for the ${}^3\Sigma_u^+$ symmetry. Numerical difficulties prevented the production of meaningful ${}^1\Sigma_g^+$ solutions for $R < 5.0$. Our eigenvalue program produced obviously spurious solutions to Eq. (7) with energies comparable to those of the molecular eigenstates of interest, thus producing spurious avoided curve crossings. The spacings between points varied considerably across the entire radial range, but were typically 2.0 for $R > 34.0$ and 0.1 for $R < 6.0$. Much smaller spacings were sometimes used near avoided energy curve crossings.

C. Results of eigenstate calculations

We now present the results of our computations of the ${}^1\Sigma_g^+$ and ${}^3\Sigma_u^+$ eigenstates and energies of the Ba_2^{++} system.

Figure 1 shows our energy curves for the ${}^1\Sigma_g^+$ eigenstates. For this discussion we label the curves and states wtih positive integers, in energetic order. Curve 1 represents the state in which, at infinite R, both Ba^+ ions are in their ground states. Curve 2 represents the state in which, at infinite R, and Ba^+ ion is in its ground state and the other ion is excited to its lowest ${}^2P$ state. Curve 3 represents the lowest electron-transfer state, in which at infinite R the molecular system resolves itself into a neutral Ba atom and a Ba^{++} ion, each in their respective ground states. Curves 4, 5, and 6 represent, at infinite R, higher excitations of the two Ba^+ ions. None of these three curves represents an electron-transfer state.

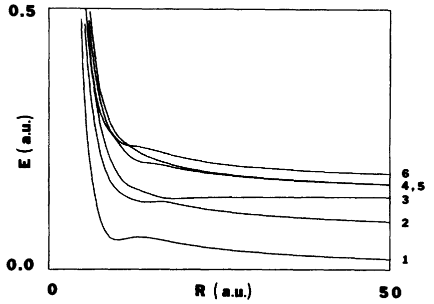

FIG. 1. Energy curves for the ${}^1\Sigma_g^+$ eigenstates of Ba_2^{++}. The energy of the electron-transfer state, state 3, is almost constant for larger R. The other energies behave as $1/R$. States 4 and 5 are degenerate for larger R.

Figure 2 shows our energy curves for the ${}^3\Sigma_u^+$ eigenstates. At infinite R, five of the six energies become equal to five of the six ${}^1\Sigma_g^+$ energies, and represent physically equivalent states of the separated Ba^+ ions. The electron-transfer state, however, is now represented by curve 6 rather than by curve 3, because at infinite R the neutral Ba atom cannot be in its ground state for the triplet spin symmetry.

Table II lists our computed energies for infinite R, relative to the ground state, and compares them with tabulated experimental energies.[10] Also listed are the spectroscopic designations of the two separated ion states comprising each molecular eigenstate. The agreement between theory and experiment is not particularly good; the theory tends to underestimate the relative energies by approximately 20%. Also, the theory fails to produce the correct ordering of the three

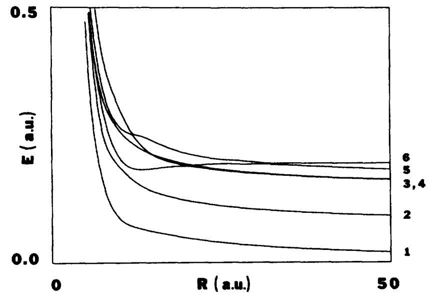

FIG. 2. Energy curves for the ${}^3\Sigma_u^+$ eigenstates of Ba_2^{++}. State 6 is the electron-transfer state. States 3 and 4 are degenerate for larger R.

TABLE II. Comparison between theoretical and experimental energies of Ba_2^{++} eigenstates for infinite internuclear separation.

Level			Energies (a.u.)	
$^1\Sigma_g^+$	$^3\Sigma_u^+$	Spectroscopic designation	Theor.	Expt.
	6	$[6p\,^3P(\mathrm{Ba})][5p^6\,^1S(\mathrm{Ba}^{++})]$	0.198	0.236
6	5	$[7s\,^2S(\mathrm{Ba}^+)][6s\,^2S(\mathrm{Ba}^+)]$	0.164	0.193
5	4	$[6p\,^2P(\mathrm{Ba}^+)][6p\,^2P(\mathrm{Ba}^+)]$	0.144	0.195
4	3	$[6p\,^2P(\mathrm{Ba}^+)][6p\,^2P(\mathrm{Ba}^+)]$	0.144	0.195
3		$[6s^2\,^1S(\mathrm{Ba})][5p^6\,^1S(\mathrm{Ba}^{++})]$	0.139	0.176
2	2	$[6p\,^2P(\mathrm{Ba}^+)][6s\,^2S(\mathrm{Ba}^+)]$	0.072	0.098
1	1	$[6s\,^2S(\mathrm{Ba}^+)][6s\,^2S(\mathrm{Ba}^+)]$	0.000	0.000

highest charge-equal levels. The level in which one Ba^+ ion is excited to the $(7s, {}^2S)$ state should lie slightly below the degenerate levels in which both ions are excited to the $(6p, {}^2P)$ state, rather than above them. Near the end of this section, we discuss the expected effects of these discrepancies on our computational study of the $Ba^+ + Ba^+$ collision.

The most important features of our $^1\Sigma_g^+$ curves are the broad avoided crossing between curves 1 and 2 at $R = 13.50$, and the close avoided crossing between curves 2 and 3 at $R = 17.00$. We anticipate that, during the collision, transition rates will be significant only between these pairs of states, and only when the internuclear separation passes through these R values. For impact parameters b much greater than 13.50, few transitions should occur. For smaller b values, electron transfer should occur by the following mechanism. Excitation to level 2 should occur when the approaching nuclei pass through $R = 13.50$, and again when the nuclei pass through that separation while receding from each other. Systems excited to level 2 should then make transitions to level 3 when the receding nuclei pass through $R = 17.00$. Because we expect the electron-transfer probability to be significant for b values as large as 13.50, the corresponding cross section (in units of πa_0^2) could be as large as $(13.50)^2 \simeq 180$.

The most important features of our $^3\Sigma_u^+$ curves are the *absence* of any avoided crossing between curves 1 and 2, except possibly for very small R values, and the extremely close avoided crossings involving the four upper curves. The crossings at $R = 31.75$ (curves 5 and 6), $R = 20.75$ (curves 4 and 5), and $R = 20.00$ (curves 3 and 4) are particularly significant. Because of the absence of avoided crossings between curves 1 and 2, we expect that, during the collision, transition rates from state 1 to state 2 will be very small unless the nuclei approach closer than about 10.00 a.u. and pass through the highly repulsive region of the energy curves. For small impact parameters, we expect that some transitions to state 2 will occur. Transitions to state 3 will then occur when the receding nuclei pass through the region inside the local minimum in curve 3, at $R = 13.00$. As the nuclei recede further the system should pass through the close avoided crossings diabatically. Most molecules excited to state 3 at small separations will thus move to state 6 at infinite separation, and very few will move to states 3, 4, and 5. We expect that the electron-transfer cross section for triplet collisions will be considerably smaller than that for singlet collisions.

Our $^3\Sigma_u^+$ curves also show extremely close avoided crossings at $R = 14.75$ (curves 4 and 5), and at $R = 11.875$ (curves 5 and 6). These features could affect the electron-transfer process if significant excitation to the upper three states occurs when the nuclei pass through the repulsive region.

We expect that our theory's average 20% underestimate of the infinite R relative energies will produce an overestimate of the electron-transfer cross sections, of similar magnitude. Because of this energy underestimate, the important avoided curve crossings will occur at R values larger than those at which they should occur. The energy gaps at the avoided crossings, however, should not be seriously affected. Therefore, the maximum impact parameter for which the internuclear separation passes through the important crossings during the collision is increased, but the transition rates while passing these regions are not seriously changed.

We could, of course, arbitrarily add constant values to the energies $E_\mu(R)$ in order to match exactly the infinite R experimental energies, as is often done with energy curves presented in the literature. In the present case, however, such an adjustment would not alter the slightly erroneous radial positions of the avoided crossings, but would drastically and unphysically increase the energy gaps at these crossings. The transition rates while passing these regions during the collision would then be unrealistically altered.

The erroneous ordering of the three upper charge-equal levels should not seriously affect our collision results. For singlet collisions, these levels all lie above the electron-transfer level and do not interact very strongly with it except perhaps for very small R. For triplet collisions, these levels lie below the electron-transfer level, but because the avoided crossings involving these levels are so extremely close, the erroneous ordering should not affect the transfer mechanism discussed in this section.

III. COLLISIONAL COUPLING MATRIX ELEMENTS

A. Exact expressions

We first manipulate Eqs. (5) and (6) into forms suitable for direct numerical use. We make the change of variables

$$z = vt$$

and write the coupled differential equations as

$$\frac{dc_\mu}{dz} = \sum_\nu K_{\mu\nu}(z)c_\nu(z)\,, \tag{9}$$

$$K_{\mu\nu}(z) = -\left\langle \Phi_\mu \middle| \left(\frac{d}{dz} + \frac{i}{v}\hat{H}(\vec{\mathrm{R}})\right) \middle| \Phi_\nu \right\rangle . \tag{10}$$

Our notation suppresses the dependence of c_μ and $K_{\mu\nu}$ on the collision speed v and the impact parameter b.

For the translation factor appearing in Eq. (4) we initially choose the form appropriate when working in a molecular eigenstates basis[11]:

$$\begin{aligned} \tau(\vec{\mathrm{R}},t) &= \prod_j \tau_j(\vec{\mathrm{R}},t)\,, \\ \tau_j(\vec{\mathrm{R}},t) &= \exp[i\tfrac{1}{2}f(\vec{\mathrm{r}}_j,\vec{\mathrm{R}})\vec{\mathrm{v}}\cdot\vec{\mathrm{r}}_j - \tfrac{1}{8}v^2 t]\,. \end{aligned} \tag{11}$$

We refer to τ_j as the *one-electron translation factor*. $\vec{\mathrm{r}}_j$ is the position of the jth electron, and $\frac{1}{8}v^2$ is the kinetic energy associated with the electron's overall translation at speed $\frac{1}{2}v$. The function $f(\vec{\mathrm{r}},\vec{\mathrm{R}})$ is chosen for mathematical convenience. It can be any function, differentiable to second order, satisfying the following conditions.

(i) f is invariant under rotation about $\vec{\mathrm{R}}$ axis.

(ii) f is antisymmetric under inversion of $\vec{\mathrm{r}}$.

(iii) $f(\vec{\mathrm{r}},\vec{\mathrm{R}}) \simeq \pm 1$ if R is larger than the atomic diameter and $|\vec{\mathrm{r}} \mp \frac{1}{2}\vec{\mathrm{R}}|$ is smaller than the atomic radius.

The first two conditions are simply consequences of the molecular symmetry. The third condition expresses the fundamental requirement that, for large internuclear separations, the wave function $\Psi(\vec{\mathrm{R}},t)$ must properly represent the uniform spatial motion of the electronic cloud around each nucleus. Further conditions on f are discussed by the original authors.[11] In the present work we choose no specific form for f.

By substituting Eqs. (4) and (11) into (10), we obtain, after straightforward but lengthy manipulation, an expression for $K_{\mu\nu}(z)$:

$$K_{\mu\nu}(z) = \exp[i\beta_{\mu\nu}(z)/v][K^0_{\mu\nu}(z) + ivK^1_{\mu\nu}(z)]\,, \tag{12}$$

where K^0 and K^1 are independent of v, and real:

$$\beta_{\mu\nu}(z) = \int_0^z [E_\mu(R') - E_\nu(R')]dz'\,,$$

$$R' = [(z'^2 + b^2)]^{1/2}\,,$$

$$K^0_{\mu\nu}(z) = -(z/R)\langle d/dR\rangle_{\mu\nu} - N(b/R^2)\langle i\hat{J}^j_y\rangle_{\mu\nu} - N(z/R)\langle\hat{F}_j(\hat{z})\rangle_{\mu\nu} - N(b/R)\langle\hat{F}_j(\hat{x})\rangle_{\mu\nu}\,, \tag{13}$$

$$\hat{F}_j(\hat{s}) = \tfrac{1}{4}\nabla^2_j[(\vec{\mathrm{r}}_j\cdot\hat{s})f(\vec{\mathrm{r}}_j,R\hat{z})] + \tfrac{1}{2}\{\vec{\nabla}_j[(\vec{\mathrm{r}}_j\cdot\hat{s})f(\vec{\mathrm{r}}_j,R\hat{z})]\}\cdot\vec{\nabla}_j\,,$$

$$\begin{aligned} K^1_{\mu\nu}(z) = {} & \tfrac{1}{8}N\delta_{\mu\nu} - \tfrac{1}{8}N(b/R)^2\langle[\vec{\mathrm{G}}_j(\hat{x})]^2\rangle_{\mu\nu} + \tfrac{1}{2}N(bz/R^3)\langle\hat{Q}_j(\hat{z},i\hat{J}_y{}^j)\rangle_{\mu\nu} + \tfrac{1}{2}N(b^2/R^3)\langle\hat{Q}_j(\hat{x},i\hat{J}_y{}^j)\rangle_{\mu\nu} \\ & - \tfrac{1}{8}N(z/R)^2\langle\{[\vec{\mathrm{G}}_j(\hat{z})]^2 + 4\hat{Q}_j(\hat{z},\partial/\partial R)\}\rangle_{\mu\nu} - \tfrac{1}{4}N(bz/R^2)\langle[\vec{\mathrm{G}}_j(\hat{z})\cdot\vec{\mathrm{G}}_j(\hat{x}) + 2\hat{Q}_j(\hat{x},\partial/\partial R)]\rangle_{\mu\nu}\,, \end{aligned} \tag{14}$$

$$\vec{\mathrm{G}}_j(\hat{s}) = \vec{\nabla}_j[(\vec{\mathrm{r}}_j\cdot\hat{s})f(\vec{\mathrm{r}}_j,R\hat{z})]\,,$$

$$\hat{Q}_j(\hat{s},\hat{O}) = (\vec{\mathrm{r}}_j\cdot\hat{s})[\hat{O}f(\vec{\mathrm{r}}_j,R\hat{z})]\,.$$

In all of the above expressions, N is the number of electrons and $\vec{\mathrm{r}}_j$ is the position of any one electron. $\hat{J}^j_y$ is the y component of the orbital angular momentum of the jth electron. The operator d/dR in Eq. (13) differentiates both the coefficients $a(R)$ and the TSF's $\phi(R)$ in Eq. (8). Also, in Eqs. (13) and (14),

$$\langle\hat{O}\rangle_{\mu\nu} = \langle\psi_\mu|\hat{O}|\psi_\nu\rangle\,.$$

We strongly emphasize that, by writing our coupling matrix elements in the form chosen, we have gained a very important computational advantage. All of the individual matrix elements $\langle\hat{O}\rangle_{\mu\nu}$ appearing in Eqs. (13) and (14) are expressed in terms of wave functions and operators which depend only on the internuclear distance and not on the molecular orientation. Therefore, all quantities requiring laborious computation are functions of only one independent variable R. Their numerical values can be tabulated once and then used in all integrations of Eq. (9). The b dependence of $K_{\mu\nu}$ enters only through the energy difference integral $\beta_{\mu\nu}(z)$ and through the simple factors (z/R), (b/R), etc., appearing in Eqs. (13) and (14). The v dependence enters only as written explicitly in Eq. (12).

B. Simplifications and approximations

We computed values of $K_{\mu\nu}(z)$ using several simplifications and approximations rather than using Eqs. (12) through (14) exactly. We have presented the exact expressions because, to the best of our knowledge, such expressions in terms of the orientation-independent nonrotated molecular eigenstates have not previously appeared in the literature in a form suitable for direct computational use.

First, because ψ_μ and ψ_ν are Σ states, several terms in K^0 and K^1 are exactly equal to zero. The matrix elements of $i\hat{J}^j_y$, $\hat{F}_j(\hat{x})$, $\hat{Q}_j(\hat{z}, i\hat{J}^j_y)$, and $[\vec{G}_j(\hat{z}) \cdot \vec{G}_j(\hat{x}) + 2\hat{Q}_j(\hat{x}, \partial/\partial R)]$ all vanish in the present case.

Second, we assumed that ivK^1 was small in magnitude compared with K^0 and could be neglected. For small speeds v this approximation is, of course, always valid. But for collision energy 100 keV, for example, $v = 0.242$ for the $Ba^+ + Ba^+$ system, which is small but not negligibly so. Our neglect of the nonzero terms of K^1 therefore requires further justification.

If $f(\vec{r}, \vec{R})$ is chosen properly then, for sufficiently large R and for $\vec{r}_j$ near either nuclear position, the terms $[\vec{G}_j(\hat{x})]^2$ and $[\vec{G}_j(\hat{z})]^2$ combine together to form a very nearly constant operator $-\frac{1}{8}N\delta_{\mu\nu}$, which cancels the leading term in K^1. The terms $\hat{Q}_j(\hat{x}, i\hat{J}^j_y)$ and $\hat{Q}_j(\hat{z}, \partial/\partial R)$ vanish because in both cases the differential operator acting on $f(\vec{r}_j, R)$ produces a result that becomes small rapidly near the nuclear positions as R becomes large. Thus, because all parts of K^1 are small for reasonably large R, our neglect of ivK^1 remains valid for intermediate v values.

Third, the first term of $\hat{F}_j(\hat{z})$ in K^0 vanishes for large R, again because the differential operator involved produces a small result near the nuclei for large R.

Fourth, we consider that part of $\langle d/dR \rangle_{\mu\nu}$ generated by differentiation of the TSF's. This function consists of two terms: The first generated by differentiation of the TSF's R-dependent normalization factor, and the second generated by differentiation of the AO's from which the TSF is constructed. We determined that the first term is negligible by actually computing its values on the coarse grid. The second term can be shown, by the following argument, to very nearly cancel the second term of $\hat{F}_j(\hat{z})$. For sufficiently large R, the second term of $\hat{F}_j(\hat{z})$ behaves as $\pm\frac{1}{2}\partial/\partial z_j$ near either nuclear position. But the AO's are functions of the arguments $(\vec{r}_j \mp \frac{1}{2}R\hat{z})$. Therefore, near either nuclear position, the d/dR operator is equivalent to $\mp\frac{1}{2}N\partial/\partial z_j$ and is canceled by the second term of $N\hat{F}_j(\hat{z})$.

Thus, all that remains of our coupling matrix elements is that part of $\langle d/dR \rangle_{\mu\nu}$ generated by differentiating $a_\nu(R)$:

$$K^0_{\mu\nu}(R) \simeq -(z/R)\tilde{D}_{\mu\nu}(R) ,$$
$$\tilde{D}_{\mu\nu}(R) = \sum_{mn} a_{m\mu}(R) S_{mn}(R) da_{n\nu}(R)/dR . \qquad (15)$$

The approximations described above are not equivalent to complete neglect of the translation factor. Rather, they simply reflect the fact that, for reasonably large internuclear separations, the effects of the Schneiderman-Russek translation factor[11] must be physically equivalent to those of the simpler Bates-McCarroll factor.[6] The latter is used in atomic-basis collision calculations rather than in molecular-basis work. In calculations using the Bates-McCarroll factor, the electronic kinetic energy associated with the overall translational motion of the colliding atoms disappears exactly from the diagonal elements of the collisional coupling matrix. Our approximate cancellation of $-\frac{1}{8}N\delta_{\mu\nu}$ by $[\vec{G}_j(\hat{x})]^2$ and $[\vec{G}_j(\hat{z})]^2$ embodies this same effect. In Bates-McCarroll calculations, coupling terms generated by differentiation of the atomic-basis functions with respect to nuclear position are exactly canceled by terms produced by a single differentiation with respect to the electron coordinates. Without this cancellation, the calculations would make a totally unphysical prediction of large transition rates even in the limit of infinite internuclear distance. Our approximate cancellation of the second term of $N\hat{F}_j(\hat{z})$ by part of $\langle d/dR \rangle_{\mu\nu}$ embodies this same effect. The other neglected terms in our coupling matrix are nonzero only because the wavelength associated with the Schneiderman-Russek translation factor is not constant over the volume of either colliding atom. However, except for fairly small internuclear separations, this variation over each atom's volume is very slight and vanishes completely in the infinite separation limit. Coupling terms produced by this variation must also become negligible.

C. Numerical methods

The integrals $\beta_{\mu\nu}$ were obtained by first interpolating the energies $E_\mu(R)$ and then analytically integrating. The interpolations were constructed using the energy values computed on the fine grid. On each fine grid interval $E_\mu(R)$ was assumed linear in R.

In computing $\tilde{D}$, the derivatives da/dR could be obtained by directly interpolating the $a(R)$ values computed on the fine grid. However, as mentioned in Sec. II A, the coefficients often vary quite rapidly, especially near avoided curve crossings, so that they cannot be interpolated reliably. We instead used a procedure which produced *exact* values of da/dR in terms of the interpolated $H(R)$ and $S(R)$ matrices, thus exploiting further these matrices' relatively slow and smooth variation with R. By differentiating the matrix eigenvalue equation (7) with respect to R and requiring that the eigenvector's norm not vary with R, an expression for da/dR is easily obtained. It then follows that

$$\tilde{D}_{\mu\nu}(R)=\begin{cases}\dfrac{a_\mu^T(R)[E_\nu(R)S'(R)-H'(R)]a_\nu(R)}{E_\mu(R)-E_\nu(R)}\,, & \nu\neq\mu\\[2ex] -\tfrac{1}{2}a_\mu^T(R)S'(R)a_\mu(R)\,, & \nu=\mu\,.\end{cases}\tag{16}$$

The derivatives $S'(R)$ and $H'(R)$ were computed using the interpolations for $H(R)$ and $S(R)$ described in Sec. II B. These interpolations must have continuous *second* derivatives, as asserted previously. Otherwise, the use of $H'(R)$ and $S'(R)$ in computing $\tilde{D}$ would cause unphysical cusps to appear at the coarse grid points. Our procedure, which avoids direct interpolation of da/dR in computing $\tilde{D}$, is another technique valuable in future treatments of large colliding systems.

Because $\tilde{D}$ is not anti-Hermitian, we replace the approximation (15) with

$$K^0_{\mu\nu}(z)\simeq-(z/R)D_{\mu\nu}(R)\,,$$

$$D_{\mu\nu}(R)=\tfrac{1}{2}[\tilde{D}_{\mu\nu}(R)-\tilde{D}_{\nu\mu}(R)]\,.$$

The original K^0 matrix [(Eq. (13)] is exactly anti-Hermitian. Because $\langle d/dR\rangle_{\mu\nu}$ is also exactly anti-Hermitian but $\tilde{D}$ is not, the matrix consisting of those parts of $\langle d/dR\rangle_{\mu\nu}$ generated by differentiation of the TSF also deviates from anti-Hermiticity. Our approximation that this matrix cancels the second term of $\hat{F}_j(\hat{z})$ [Eq. (13)], which *is* anti-Hermitian, is the approximation that causes the loss of anti-Hermiticity. In Sec. III D we show that $\tilde{D}$'s deviation from anti-Hermiticity is not excessively serious for larger R values.

D. Computational results

Using Eq. (16), we computed numerical values of $\tilde{D}_{\mu\nu}(R)$ and $D_{\mu\nu}(R)$, for all R values included in the fine grid, for couplings among the six lowest $^1\Sigma_g^+$ states and among the six lowest $^3\Sigma_u^+$ states. Figures 3, 4, and 5 show plots of $D_{\mu\nu}(R)$ for couplings among the three lowest $^1\Sigma_g^+$ states.

Coupling element $D_{31}(R)$ is considerably smaller in magnitude than $D_{21}(R)$ and $D_{32}(R)$, for most R. Therefore, direct transitions from state 1 to state 3 should not be significant. Element $D_{21}(R)$ shows a broad valley with its minimum at $R=13.00$, corresponding to the broad avoided crossing between energy curves 1 and 2 in Fig. 1. Element $D_{32}(R)$ shows a sharp peak at $R=17.00$, corresponding to the close avoided crossing between energy curves 2 and 3. In addition, $D_{32}(R)$ shows a narrow valley at $R=11.25$. This valley reflects changes in $\psi_2(R)$ due to its interaction with state 1 near the broad avoided crossing between curves 1 and 2. The positions of these peaks and valleys at R values corresponding to avoided curve crossings supports the qualitative conclusions of Sec. II C.

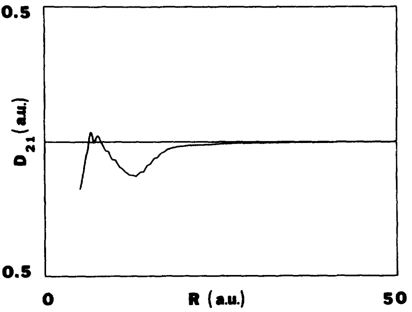

FIG. 3. Singlet collisional coupling matrix element $D_{21}(R)$.

The $D_{\mu\nu}(R)$ matrix elements for the $^3\Sigma_u^+$ states, which are not plotted here, show extremely sharp peaks or valleys in elements $D_{65}(R)$, $D_{54}(R)$, and $D_{43}(R)$ at $R=31.75$, 20.75, and 20.00, respectively. These features correspond to the extremely close avoided crossings discussed in Sec. II C, involving the four upper energy curves (see Fig. 2). Their extreme sharpness and narrowness supports our *a priori* expectation that, once excited to a higher state at smaller R, the system should pass through these avoided crossings diabatically. The structure of the coupling elements for smaller R is confusing, and does not clearly indicate what excitation pattern should dominate at small R.

We also computed numerical values of the function

$$T_{\mu\nu}(R)=\tfrac{1}{2}[\tilde{D}_{\mu\nu}(R)+\tilde{D}_{\nu\mu}(R)]\,,$$

in order to test the seriousness of the D matrix's

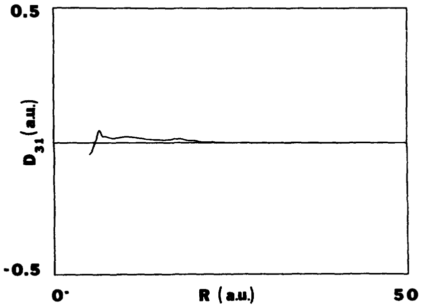

FIG. 4. Singlet collisional coupling matrix element $D_{31}(R)$.

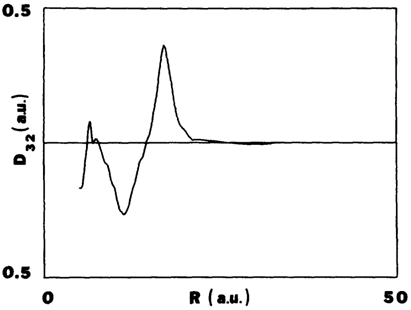

FIG. 5. Singlet collisional coupling matrix element $D_{32}(R)$.

deviation from anti-Hermiticity. If $\tilde{D}$ were exactly anti-Hermitian, then T would be a zero matrix. Figure 6 shows the common logarithms of $|D_{21}|$ and $|T_{21}|$ plotted as functions of R, for singlet coupling. Clearly, T_{21} vanishes much more rapidly as R becomes large than does D_{21}. Also, T_{21} never becomes larger in magnitude than about one-third of the D_{21} magnitude, even for R values near the important broad coupling valley (which appears as a rounded peak in this logarithmic plot). Our computations showed that all of the important $T_{\mu\nu}$ functions behaved similarly. We conclude that our replacement of the matrix $\tilde{D}$ with the anti-Hermitian matrix D will not cause serious error in our collision dynamics results.

IV. Collision dynamics

A. Procedure

Using the coupling matrix elements computed as described in Sec. III, we have numerically integrated the coupled differential equations (9), for both singlet collisions and triplet collisions. The integrations were performed for energies ranging from 25 to 500 keV; these energy range limits correspond to speeds of 0.121 and 0.540, respectively. The singlet integrations were performed for impact parameters ranging from 5 to 20; the triplet range was 3 to 20. For the triplet computations, all six states represented in Fig. 2 were included in the coupling. Initially, the singlet computations included only the three lowest states represented in Fig. 1. Additional computations were then performed which included all six singlet states, in order to test the sensitivity of the singlet electron-transfer process to the inclusion of the higher states. All computations used the Runge-Kutta method.

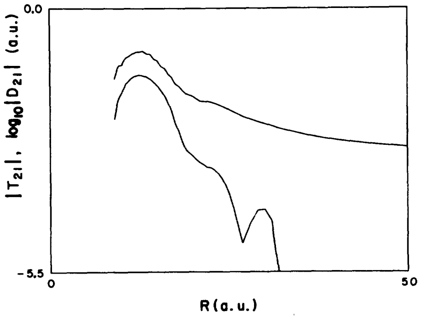

FIG. 6. The common logarithms of $|D_{21}(R)|$ (upper curve) and $|T_{21}(R)|$ (lower curve).

In performing these computations, the functions $E_\mu(R)$ and $D_{\mu\nu}(R)$ were assumed linear in R on each fine grid interval. Figures 1–5 were plotted assuming this same interpolation scheme. These plots clearly demonstrate that such a linear interpolation produces acceptably smooth results on the fine grid.

For each spin degeneracy, collision speed, and final state μ, we computed two values for the associated cross section, in units of πa_0^2. We denote these values $\sigma_\mu^l(v)$ and $\sigma_\mu^i(v)$:

$$\sigma_\mu^l(v) \equiv 2\int_{b_0}^{b_x} bP_\mu(v,b)db ,$$

where $b_x = 20$, and $b_0 = 5$ for singlet collisions and 3 for triplet collisions. $P_\mu(v,b)$ is our computed transition probability. Clearly, σ_μ^l is an estimated lower limit on the cross-section value.

To compute σ_μ^i, we extrapolated the functions $E_\mu(R)$ and $D_{\mu\nu}(R)$ to $R=0$ and performed numerical integrations of the coupled equations for impact parameters from b_0 down to zero:

$$\sigma_\mu^i(v) = \sigma_\mu^l(v) + 2\int_0^{b_0} bP_\mu(v,b)\,db ,$$

and is a cross-section value that includes an estimate of the contribution due to small-impact-parameter collisions. Each $E_\mu(R)$ was extrapolated to $R=0$ as a second-order polynomial in R with continuous slope at $R=b_0$ and zero slope at $R=0$. Each $D_{\mu\nu}(R)$ was extrapolated as a third-order polynomial with zero slope at $R=b_0$ and approaching zero linearly as $R\to 0$. These extrapolations are very approximate but their purpose is to provide no better than a very rough estimate of the transition probabilities at small impact parameters.

B. Singlet results

Figure 7 illustrates a sample of our singlet collision, three-state coupling results. The curves represent the system's probabilities $P_\mu(v,b)$ of finishing the collision in each of the three lowest $^1\Sigma_g^+$ states, as functions of impact parameter b, for fixed collision energy 100 keV.

For the largest b values, the probability P_1 of remaining in state 1 approaches unity and the

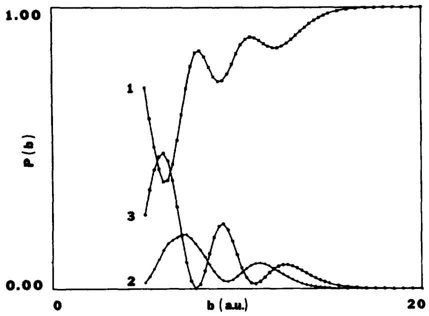

FIG. 7. Singlet collisional excitation probabilities as functions of impact parameter, for energy 100 keV.

probabilities of transition to states 2 and 3 approach zero. As anticipated in our discussion of Sec. II C, significant loss of probability from the initial channel does not occur until *b* decreases to around 13. For *b* values near 13, the colliding system passes once tangentially through the broad valley in coupling matrix element D_{21} (see Fig. 3), giving rise to the first local minimum in P_1. For smaller *b* values, the colliding system passes twice through this valley, giving rise to an oscillatory interference pattern in P_1. As *b* varies, the distance traveled between these two passages varies, so that transitions occurring during the second passage sometimes interfere constructively and sometimes destructively with transitions occurring during the first. The oscillations in curves P_2 and P_3 are of course due to this same interference effect. Our computations show this effect occurring for all energies, with the spacing between oscillation peaks increasing with collision energy.

Figures 8 and 9 illustrate the system's behavior during the collision, as a function of distance z along the collision path, for energy 100 keV, and impact parameters 6.00 and 7.75. These *b* values correspond to the innermost peak and valley in curve P_3 of Fig. 7. Each curve represents the system's probability $p_\mu(z,v,b)$ of being in state μ at each point z along the collision path. The left-hand sides of the plots ($z=-20$) correspond to the collision's initial conditions: The nuclei are approaching each other from a long distance, and the probabilities p_1, p_2, and p_3 are unity, zero, and zero, respectively. The centers of the plots ($z=0$) correspond to the point of closet approach between the nuclei. The right-hand sides ($z=20$) correspond to the collision's final conditions: The nuclei are receding from each other at a long distance, and the probabilities $p_\mu(z,v,b)$ have stabilized at the values $P_\mu(v,b)$ plotted in Fig. 7 for the appropriate *b* values. The vertical dashed lines represent the points at which the system passes through the important peaks and valleys in the coupling matrix elements. In each plot, the outermost pair (extreme left and right) represents the sharp peak in D_{32} at $R=17.00$, the next pair represents the broad valley in D_{21} at $R=13.50$, and the innermost pair represents the narrow valley in D_{32} at $R=11.25$.

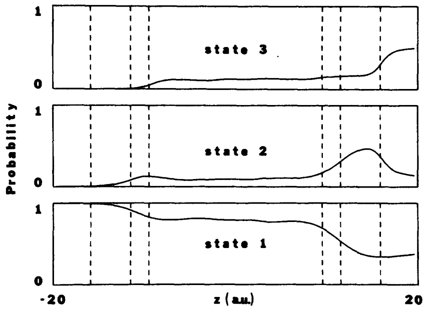

FIG. 8. Behavior of the colliding singlet system as function of position along collision path, for energy 100 keV and impact parameter 6.00. Each curve represents the system's probability of being in the state indicated, at each moment during the collision.

For both *b* values, Figs. 8 and 9 show that electron transfer occurs largely by the mechanism anticipated. Viewing the plots from left to right, we see that, as the nuclei approach, state 1 loses no probability until the system passes through the broad valley in D_{21} (second dashed line), where state 1 loses significant probability to state 2, as anticipated. As the system passes through the narrow valley in D_{32} (third dashed line), state 3 gains significant probability, an effect that was not anticipated.

As the nuclei approach still closer, pass their point of closest approach, and begin receding, the plots show that little change occurs in the probabilities until the system again passes through the important coupling peaks and valleys. As anticipated, transition rates during the collision are significant only when the system passes through the avoided crossings in the energy curves.

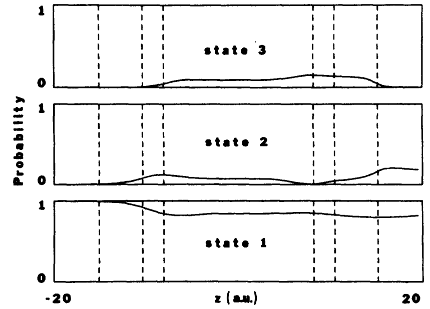

FIG. 9. Same as Fig. 8, for impact parameter 7.75.

As the receding nuclei pass through the narrow D_{32} valley and the broad D_{21} valley, different behavior occurs for the two different b values. For $b = 6.00$, state 1 loses large probability to state 2, while the probability of state 3 remains almost unchanged. For $b = 7.75$, state 2 temporarily loses almost all of its probability to states 1 and 3, and then regains it. This behavior difference is caused by the interference effect described earlier.

Finally, when the receding nuclei pass through the sharp D_{32} peak, the probability of state 1 remains almost unchanged while considerable probability is transferred between states 2 and 3, as anticipated. For $b = 6.00$, state 2 loses most of its probability to state 3, so that a large degree of electron transfer occurs. For $b = 7.75$, state 3 loses most of its probability to state 2, so that very little transfer occurs. Again, this behavior difference is caused by the interference effect described previously.

Table III lists our computed values, in units of πa_0^2, of the cross sections σ_μ^l and σ_μ^i as functions of collision energy, for $\mu = 2$ and $\mu = 3$; these values were computed using three-state coupling. The electron-transfer cross section σ_3, as the energy increases from zero, at first rapidly increases and then levels off for energies around 250 keV or higher. Above 500 keV σ_3 probably decreases, so that σ_3 exhibits a broad peak in the 250–500-keV range. For $E = 500$ keV the collision speed $v = 0.540$, so that for higher energies our neglect of the ivK^1 term in the collision coupling matrix elements is probably not valid. The ratio (σ_3^i/σ_3^l) averages 1.25 over the 250–500-keV-range, indicating that $b < 5$ collisions contribute only about 25% of the peak values of the electron-transfer cross section.

TABLE III. Computed excitation and electron-transfer cross sections, as functions of energy, for singlet collisions. These values were computed using three-state coupling.

Energy (keV)	σ_2^l	σ_2^i	σ_3^l	σ_3^i
25	1.21	2.19	2.35	3.84
50	5.52	10.82	10.69	13.45
75	8.26	17.58	15.41	19.93
100	13.10	16.00	22.94	25.38
150	18.67	20.56	28.75	35.56
200	21.29	23.91	41.81	44.64
250	23.85	25.94	51.24	54.50
300	26.92	28.46	54.64	63.74
350	30.12	31.41	55.09	70.05
400	33.17	34.51	54.84	73.20
450	35.96	37.61	54.86	74.08
500	38.50	40.63	55.35	73.65

We conclude that, for singlet collisions, the maximum electron-transfer cross section occurs for energies around 250–500 keV. Its maximum value is around 70 πa_0^2 (6.2×10^{-15} cm^2), which is much larger than the Ba$^+$ ion's geometric cross section. Most electron-transfer events involve migration by the transferred electron across distances of several ionic diameters. Because $\sigma_3 > \sigma_2$ over our entire energy range, we further conclude that singlet collisional interaction between two Ba$^+$ ions is somewhat more likely to result in electron-tranfer than in nontransfer excitation.

Table IV compares our cross sections computed using six-state coupling [$\sigma(6)$] with those computed using three-state coupling [$\sigma(3)$]. Only the estimates σ^i are listed; the σ^l are not listed.

TABLE IV. Comparison between singlet cross sections computed in three-state coupling scheme with those computed in six-state coupling scheme. The listed ratios reflect the importance of the three higher excited states.

Energy (keV)	Three-state coupling			Six-state coupling			
	σ_2^i	σ_3^i	$\sum_{\mu=2}^{3} \sigma_\mu^i$	σ_2^i	σ_3^i	$\sum_{\mu=4}^{6} \sigma_\mu^i$	$\sum_{\mu=2}^{6} \sigma_\mu^i$
50	10.82	13.45	24.27	8.44	13.00	4.01	25.45
100	16.00	25.38	41.38	16.11	21.27	6.04	43.42
200	23.91	44.64	68.56	19.51	38.05	14.29	71.85
300	28.46	63.74	92.21	25.46	52.01	18.76	96.23
400	34.51	73.20	107.71	31.05	53.68	23.69	108.41
500	40.63	73.65	114.27	35.04	58.87	25.51	119.42

Ratio	Maximum	Minimum	Average
$[\sigma_2^i(6)/\sigma_2^i(3)]$	1.01	0.78	0.88
$[\sigma_3^i(6)/\sigma_3^i(3)]$	0.97	0.73	0.83
$\left(\sum_{\mu=2}^{6} \sigma_\mu^i(6) \Big/ \sum_{\mu=2}^{3} \sigma_\mu^i(3)\right)$	1.05	1.01	1.04

Also listed are various ratios between six-state and three-state cross sections. The ratio $[\sigma_2^i(6)/\sigma_2^i(3)]$ averages 0.88 and $[\sigma_3^i(6)/\sigma_3^i(3)]$ averages 0.83, so that inclusion of the three upper ${}^1\Sigma_g^+$ states in the collisional coupling reduces the magnitudes of our cross sections somewhat, but does not alter our qualitative conclusions concerning the physical characteristics of the electron-transfer process. The ratio $(\sum_\mu \sigma_\mu^i(6)/\sum_\mu \sigma_\mu^i(3))$ averages 1.04, so that inclusion of the higher ${}^1\Sigma_g^+$ states has almost no effect on the *total* cross section for collisional excitation from the ground state. This conclusion is reasonable, because the ground state couples only very weakly with these higher states.

C. Triplet results

Figures 10(a) and 10(b) illustrate a sample of our triplet collision results. The curves represent the system's probabilities of finishing the collision in each of the six ${}^3\Sigma_u^+$ states, as functions of impact parameter, for energy 200 keV.

We see that significant loss of probability from state 1 does not occur until b decreases to around 9. As anticipated from our inspection of the ${}^3\Sigma_u^+$ energy curves (Fig. 2), significant excitation from state 1 does not occur unless the system passes through the higher repulsive region of the curves. The lack of avoided crossing between curves 1 and 2 at larger R prevents the occurrence of long-distance collisional excitation. The triplet and singlet collision processes differ from each other in this respect.

Figures 10(a) and 10(b) also show that, contrary to our expectations, molecules excited above level 2 at small separations do *not* predominantly move to state 6 as the nuclei recede from each other. Rather, most such molecules finish the collision in state 3.

Figures 11(a) and 11(b) illustrate the system's behavior during the collision, as a function of distance along the collision path, for energy 200 keV and impact parameter 6.00. This b value corresponds to the peak in curve P_3 of Fig. 10(a). The outermost, intermediate, and innermost pairs of vertical dashed lines represent the points at which the system passes through the avoided curve crossings at $R=20.00$, 14.75, and 11.875, respectively.

Figures 11(a) and 11(b) show that, when the nuclei are very close together, major excitation to state 6 occurs. The similarity in shape of the p_6 curve and the p_2 curve near $z=0$ suggests that state 6 is being populated by direct transitions from state 2, while simultaneously state 2 is

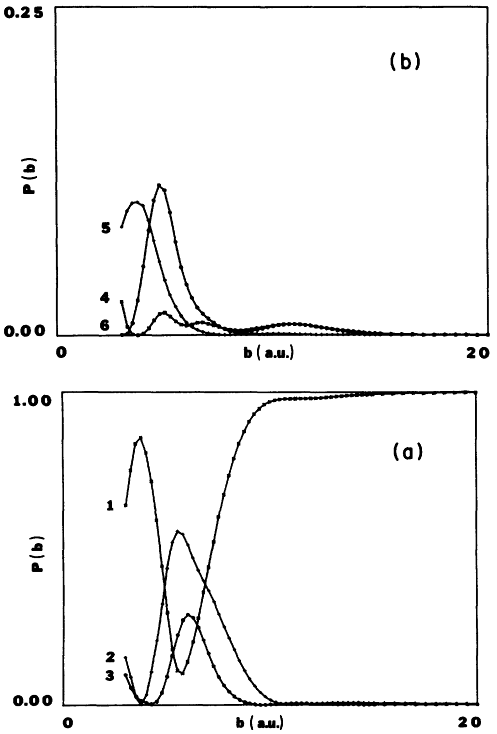

FIG. 10. (a) Triplet collisional excitation probabilities as functions of impact parameter, for energy 200 keV. Probabilities are plotted for states 1, 2, and 3 only. (b) Same as (a), but for states 4, 5, and 6. Note change in scale of ordinate.

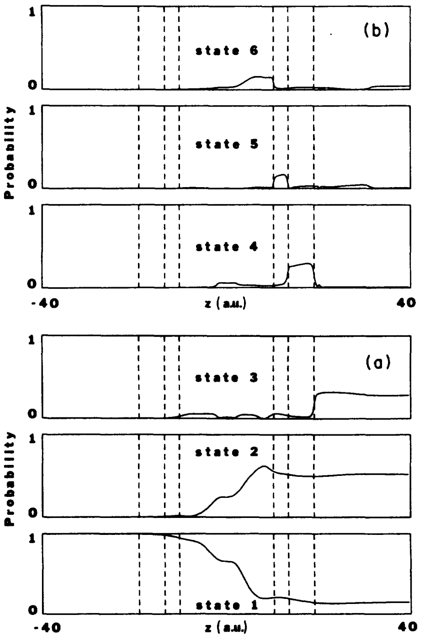

FIG. 11. (a) Behavior of colliding triplet system as function of position along collision path, for energy 200 keV and impact parameter 6.00. Probabilities are plotted for states 1, 2, and 3 only. (b) Same as (a), but for states 4, 5, and 6.

being populated by transitions from state 1. Contrary to expectations, the system emerges from the highly repulsive region of the energy curves (Fig. 2) with state 6 rather than state 3 the most heavily populated of the four upper states. As the nuclei recede and the system passes diabatically through the avoided crossings at $R=11.875$, 14.75, and 20.00, this probability in state 6 first flows sharply to state 5, then from state 5 to state 4, and then from state 4 to state 3, where it remains as the nuclei recede to infinity. Very little electron transfer occurs because very little excitation to state 3 occurs near $z=0$. Consequently, very little probability flows diabatically to state 6 as $z\rightarrow\infty$. Our failure to anticipate direct excitation to state 6 from a much lower state, while the nuclei are very close, led to our erroneous prediction stated in Sec. II C that most molecules excited above state 2 would finish the collision in state 6.

Table V lists our computed values of the cross sections σ_μ^l and σ_μ^i as functions of collision energy, for $\mu=2$ and $\mu=6$. These values were computed using six-state coupling. The electron-transfer cross section σ_6 increases monotonically but rather slowly with energy over the entire energy range. As anticipated, its values are considerably smaller than the singlet electron-transfer cross-section values, typically by a factor of around 8. The ratio (σ_6^i/σ_6^l) averages 1.04 on the 250–500-keV energy range, indicating that $b<3$ collisions contribute only about 4% of the transfer cross-section value.

The σ_6 values tabulated indicate that the cross section probably peaks broadly in the 500–1000-keV range. We thus conclude that, for triplet collisions, the maximum electron-transfer cross section occurs for energied in this range. Its maximum value is around 10–15 πa_0^2 (0.9–1.3 $\times 10^{-15}$ cm^2), which is comparable to the Ba$^+$ ion's geometric cross section. Most electron-transfer events involve migration by the electron across distances comparable to the ionic diameter. Because $\sigma_6<\sigma_2$ over our entire energy range, we further conclude that triplet collisional interaction between two Ba$^+$ ions is considerably more likely to result in nontransfer excitation than in electron transfer. These conclusions differ sharply from our conclusions concerning the singlet collision.

Table VI compares σ_2^i, σ_6^i, and the sum $\sigma_3^i+\sigma_4^i+\sigma_5^i$. For all energies this sum is much larger than σ_6^i; our failure to correctly anticipate the excitation mechanism illustrated by Fig. 11 applies over the entire energy range. Of those molecules collisionally excited to states higher than state 2, only about 28% enter the electron-transfer state.

D. Further discussion of results

Our results, as discussed in sections IV B and IV C, show that the singlet and triplet collisional electron-transfer processes differ radically from each other, both in the numerical magnitudes of the cross sections and in the physical processes leading to electron transfer. These differences occur because, in the triplet transfer process, the neutral Ba atom produced cannot be in its ground state. Therefore, an avoided crossing between the ground state and the first excited state occurs at a large separation in the singlet system, but not in the triplet system. This crossing's presence leads to the dominance of large impact parameters in singlet collisions. Its absence leads to the dominance of somewhat smaller impact parameters in triplet collisions.

Figure 12 shows the total electron-transfer cross section, computed as a statistically weighted

TABLE V. Computed excitation and electron-transfer cross sections for triplet collisions.

Energy (keV)	σ_2^l	σ_2^i	σ_6^l	σ_6^i
25	0.83	1.78	0.28	0.72
50	2.95	4.32	1.39	2.15
75	6.79	8.23	2.64	3.46
100	11.41	12.94	2.83	3.19
150	20.85	21.40	2.66	2.76
200	22.54	23.26	2.92	3.00
250	21.33	21.78	3.91	4.08
300	20.30	20.61	5.36	5.61
350	20.07	20.43	6.95	7.25
400	20.57	21.03	8.45	8.80
450	21.58	22.10	9.73	10.08
500	22.88	23.42	10.78	11.11

TABLE VI. Comparison between electron-transfer cross section and total cross section for nontransfer excitation in triplet collisions.

Energy (keV)	σ_2^i	$\sum_{\mu=3}^{5}\sigma_\mu^i$	σ_6^i
25	1.78	1.34	0.72
50	4.32	4.60	2.15
75	8.23	5.50	3.46
100	12.94	5.37	3.19
150	21.40	8.05	2.76
200	23.26	12.67	3.00
250	21.78	17.04	4.08
300	20.61	21.06	5.61
350	20.43	24.13	7.25
400	21.03	25.97	8.80
450	22.10	27.00	10.08
500	23.42	27.64	11.11

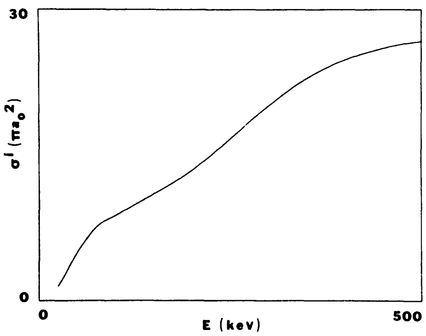

FIG. 12. The total electron-transfer cross section σ^i, computed as a statistically weighted sum of the singlet and triplet cross sections.

sum of the singlet and triplet cross sections:

$$\sigma^i(\text{total}) = 0.25\ \sigma_3^i(\text{singlet}) + 0.75\ \sigma_6^i(\text{triplet})\ .$$

As the energy increases from zero, the cross section at first increases fairly rapidly and appears to level off for energies near 500 keV. We conclude that the maximum electron-transfer cross section occurs for energies around 500 keV. Its value is around 27 $\pi a_0^2 (2.4 \times 10^{-15}\ \text{cm}^2)$. This value is somewhat larger than the Ba^+ ion's geometric cross section, and may be unacceptable for some of the envisioned HIF schemes.

ACKNOWLEDGMENT

We wish to thank Mr. Robert Vance for assistance in using the MCVB molecular quantum-mechanics computer codes. This research was supported by the United States Department of Energy under Contract No. EG-77-S-02-4379.

---

[1] Proceedings of the Heavy Ion Fusion Workshop, Argonne National Laboratory, September, 1978, Document No. ANL-79-41 (unpublished).

[2] For a review and extensive bibliography, see J. S. Briggs, Rep. Prog. Phys. 39, 217 (1976).

[3] G. A. Gallup, Int. J. Quantum Chem. 6, 761 (1972).

[4] G. A. Gallup, Int. J. Quantum Chem. 6, 899 (1972).

[5] R. Shakeshaft, J. Phys. B 5, 559 (1972).

[6] D. R. Bates and R. McCarroll, Proc. R. Soc. London, Ser. A 245, 175 (1958).

[7] J. L. Whitten, J. Chem. Phys. 44, 359 (1966).

[8] C. C. J. Roothaan, Rev. Mod. Phys. 23, 69 (1951).

[9] Robert W. Numrich and Donald G. Truhlar, J. Phys. Chem. 79, 2745 (1975).

[10] Charlotte E. Moore, *Atomic Energy Levels*, National Bureau of Standards Circular No. 467 (U.S. Dept. of Commerce, Washington D.C., 1949).

[11] S. B. Schneiderman and A. Russek, Phys. Rev. 181, 311 (1969).